RESEARCH ARTICLE

CELL SURFACE MAPPING

Microenvironment mapping via Dexter energy transfer on immune cells

Jacob B. Geri[1]*, James V. Oakley[1]*, Tamara Reyes-Robles[2]*, Tao Wang[1]*, Stefan J. McCarver[1], Cory H. White[2], Frances P. Rodriguez-Rivera[3], Dann L. Parker Jr.[3], Erik C. Hett[2], Olugbeminiyi O. Fadeyi[2]†, Rob C. Oslund[2]†, David W. C. MacMillan[1]†

Many disease pathologies can be understood through the elucidation of localized biomolecular networks, or microenvironments. To this end, enzymatic proximity labeling platforms are broadly applied for mapping the wider spatial relationships in subcellular architectures. However, technologies that can map microenvironments with higher precision have long been sought. Here, we describe a microenvironment-mapping platform that exploits photocatalytic carbene generation to selectively identify protein-protein interactions on cell membranes, an approach we term MicroMap (μMap). By using a photocatalyst-antibody conjugate to spatially localize carbene generation, we demonstrate selective labeling of antibody binding targets and their microenvironment protein neighbors. This technique identified the constituent proteins of the programmed-death ligand 1 (PD-L1) microenvironment in live lymphocytes and selectively labeled within an immunosynaptic junction.

Spatial relationships between biomolecules underpin the fundamental processes of life. In the context of cell surfaces, it has long been established that proteins are localized into defined assemblies, termed microenvironments (*1*). These substructures play a critical role in intercellular communication (*2*). As such, the capacity to precisely map these cellular landscapes should provide crucial insights into fundamental biology that will have wide-reaching implications for human health and the development of therapeutic strategies (*3*). In more specific terms, improved methods for microenvironment mapping are likely to enable discoveries in areas as wide ranging as proteomics (antibody target identification and discovering protein-protein interactions) (*4*), genomics (profiling biomolecules near genetic loci) (*5*), and neuroscience (elucidating synapse dynamics) (*6*).

In recent years, several platforms have emerged that enable the specific labeling of proteins by using the concept of spatial proximity (*7*–*9*). These technologies (APEX, SPPLAT, EMARS, and BioID) (*10*, *11*) use tethered enzymes that catalytically generate reactive open-shell or electrophilic species that target specific amino acid residues in neighboring systems. Because these intermediates have extended half-lives (0.1 ms to 60 s), they undergo diffusion at rates comparable with that of labeling (Fig. 1) (*12*). These elegant strategies have primarily been applied to the proteomic profiling and imaging of larger protein architectures such as mitochondria, lipid droplets, and nuclear pores (*13*–*15*) as well as regions such as synaptic clefts (*16*), lipid rafts (*9*), nuclear lamina (*17*, *18*), and protein clusters (*19*, *20*).

Given the intrinsic value of understanding biological systems at the microenvironment level, there remains a demand for cellular mapping technologies that operate at short range and with high precision. With this in mind, we identified a series of requirements for a suitable micromapping technology that might be used across a range of cellular constructs: (i) a catalytic manifold tolerant of aqueous conditions and biomolecules; (ii) a catalyst that can be conjugated to a range of targeting modalities—antibodies, small-molecule ligands, macromolecules, DNA, and sugars (*21*); (iii) a catalysis mechanism that can selectively activate chemical probes at a diffusion-limited rate; (iv) a readily accessible labeling probe that is only activated within 1 nm of the catalyst radius; (v) a labeling probe that is sufficiently reactive not to undergo long-range diffusion after activation; and (vi) a biomolecule-labeling mechanism that is both diffusion-limited and residue agnostic. The successful realization of these goals could, therefore, be applied within spatially restricted environments that have to date proven challenging to profile with high precision, such as the immunosynapse.

Design plan

It has long been established that carbenes readily cross-link with C–H bonds found in all biomolecules [rate constant (k) = 3.1×10^9 s^{-1}] and cannot diffuse farther than 4 nm owing to fast quenching by water [k = 3.1×10^8 s^{-1}, half-life ($T_{1/2}$) < 2 ns] (*22*, *23*). This reactivity profile renders carbenes ideal reactive intermediates for high-precision microenvironment mapping. Although diazirine-based probes have been widely applied in small-molecule target identification (*24*), the general requirement for direct excitation with ultraviolet (UV) light precludes the possibility of a target-localized activation of free diazirine substrates by using short-wavelength light. By contrast, it is well known that diazirines exhibit little to no direct absorption of blue light (410 to 490 nm) (*25*). We recently questioned whether visible light–powered iridium catalysts could sensitize diazirines by means of a Dexter energy transfer mechanism. This would allow blue light-emitting diodes (LEDs) to indirectly activate diazirines, localizing the generation of carbenes to within 0.1 nm of the photocatalyst. If that is possible, we further recognized the opportunity to apply this localized excitation to a high-precision platform for microenvironment mapping. More specifically, we envisioned a photocatalytic proximity labeling technology for carbene generation in which a spatially targeted iridium complex acts as an antenna (Fig. 1, top), absorbing the photonic energy of visible light and transferring it to a diazirine probe (Fig. 2A). Among numerous applications, we hypothesized that this approach to MicroMapping (μMap) would offer sufficient spatiotemporal resolution to profile nanoscale protein assemblies on the surface of cells.

The proposed mechanism of the transformation is outlined in Fig. 2A. First, a ground-state iridium-based photocatalyst would be excited to its S_1 state through absorption of blue (450 nm) light. Quantitative intersystem crossing to the long-lived triplet excited state (T_1) ($T_{1/2}$ = 0.2 to 3 μs) is then followed by short-range Dexter energy transfer, in which the catalyst is returned to its ground S_0 state, and diazirine is promoted to its T_1 state (*26*). The triplet diazirine undergoes elimination of N_2 to release a triplet carbene, which undergoes picosecond–time scale spin equilibration (*27*) to its reactive singlet state ($T_{1/2}$ < 1 ns) and then either cross-links with a nearby protein or is quenched by the aqueous environment. We identified four key catalyst design elements required for successful photocatalytic proximity labeling: (i) a triplet energy in excess of 60 kcal/mol, facilitating energy transfer to the diazirine substrate; (ii) a visible-light extinction coefficient (ε_{420}) greater than 1000 M^{-1} cm^{-1}, to enable the use of light sources that do not promote background diazirine photolysis; (iii) hydrophilicity for biocompatible conditions; and (iv) a suitable reactive handle for bioconjugation.

Methodology development

We first tested the feasibility of visible light–sensitized N_2 elimination from diazirines by screening a variety of photocatalysts with increasing triplet energies (Fig. 2B). Although catalysts with triplet energies below 60 kcal/mol

[1]Merck Center for Catalysis, Princeton University, Princeton, NJ 08544, USA. [2]Merck Exploratory Science Center, Merck & Co., Inc., Cambridge, MA 02141, USA. [3]Discovery Chemistry, Merck & Co., Inc., Kenilworth, NJ 07033, USA.
*These authors contributed equally to this work.
†Corresponding author. Email: olugbeminiyi.fadeyi@merck.com (O.O.F); rob.oslund@merck.com (R.C.O.); dmacmill@princeton.edu (D.W.C.M.)

did not sensitize model diazirine **1**, a catalyst with a triplet energy (E_T) exceeding this threshold {Ir[dF(CF_3)ppy]$_2$(dtbbpy)}PF_6 (**2**) (E_T = 60.1 kcal/mol) (*28*) promoted consumption of **1** under mild conditions (15 min, 25°C, 100 μM H_2O/dimethyl sulfoxide, 450 nm irradiation) in >97% yield. No reaction was observed with diazirine **1** in the absence of photocatalyst or light. We then redesigned this catalyst for biomolecular applications by increasing its water solubility through the addition of polyethylene glycol, carboxylic acid, and alkyne functional groups (**3**) (Fig. 2B). These modifications did not negatively affect its ability to sensitize N_2 elimination from **1** (supplementary materials). Diazirine sensitization could be extended to a variety of *p*- and *m*-substituted aryltrifluoromethyl diazirines bearing valuable payloads for microscopy and proteomics applications, including free carboxylic acid, phenol, amine, alkyne, carbohydrate, and biotin groups (fig. S1). The extinction coefficient of the photocatalyst (**2**) is five orders of magnitude larger than that of the diazirine (**1**) at the wavelength emitted by the blue LEDs used for sensitization (450 nm), explaining the absence of a noncatalyzed background reaction (fig. S2). Last, we assigned a short-range (Dexter) energy transfer mechanism rather than a longer-range Förster energy transfer mechanism on the basis of a lack of overlap between the absorption band of diazirine **1** and the emission band of iridium catalyst **2** even at high concentrations of **1** (0.1 M) (fig. S3). Energy transfer was highly efficient, with a rate constant of 7.9(5) × 10^7 $M^{-1}s^{-1}$ (measured through Stern-Volmer analysis; number in parentheses indicates standard deviation in trailing digit) (table S1 and figs. S4 and S5).

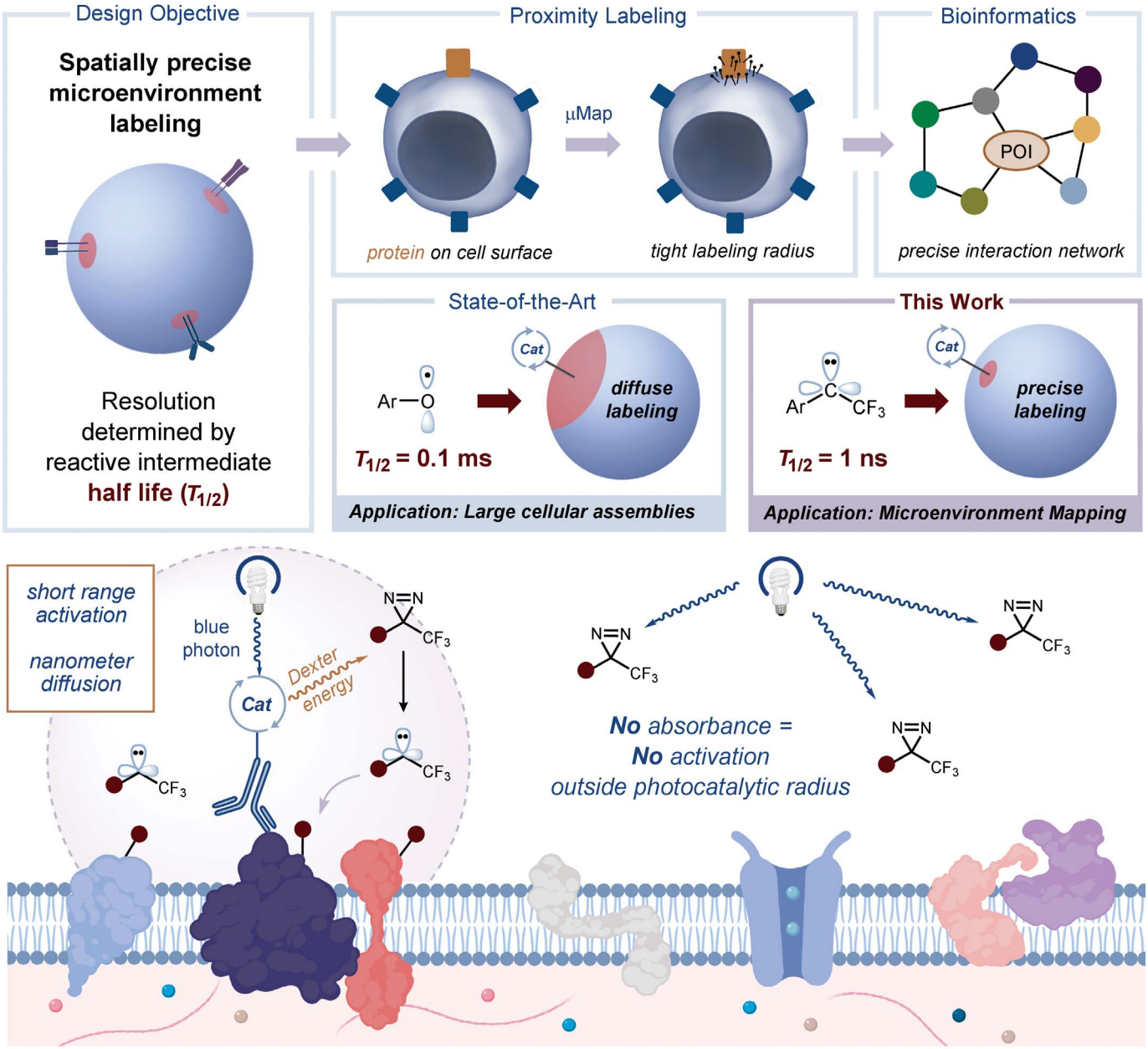

Fig. 1. High-resolution proximity-based labeling by using carbene intermediates. Spatially precise labeling enables the construction of information-rich interaction networks. (Top) The resolution of proximity-based labeling is fundamentally limited by the long solution half-life ($T_{1/2}$) of the reactive intermediates, such as phenoxyl radicals, used to label protein constituents of cell-membrane microenvironments. POI, Protein of interest. (Bottom) Using shorter-lived carbenes as reactive intermediates bypasses this limitation, enabling new applications in chemical biology.

We sought to demonstrate that carbenes generated through photocatalytic diazirine sensitization could label proteins (Fig. 2C). When a solution of bovine serum albumin (BSA) (10 μM) and a biotinylated diazirine probe **4** (100 μM) were irradiated with 375-nm light, biotinylation of BSA was detected through Western blot. When irradiated with lower-energy visible light at 450 nm, the degree of biotinylation was <0.5%

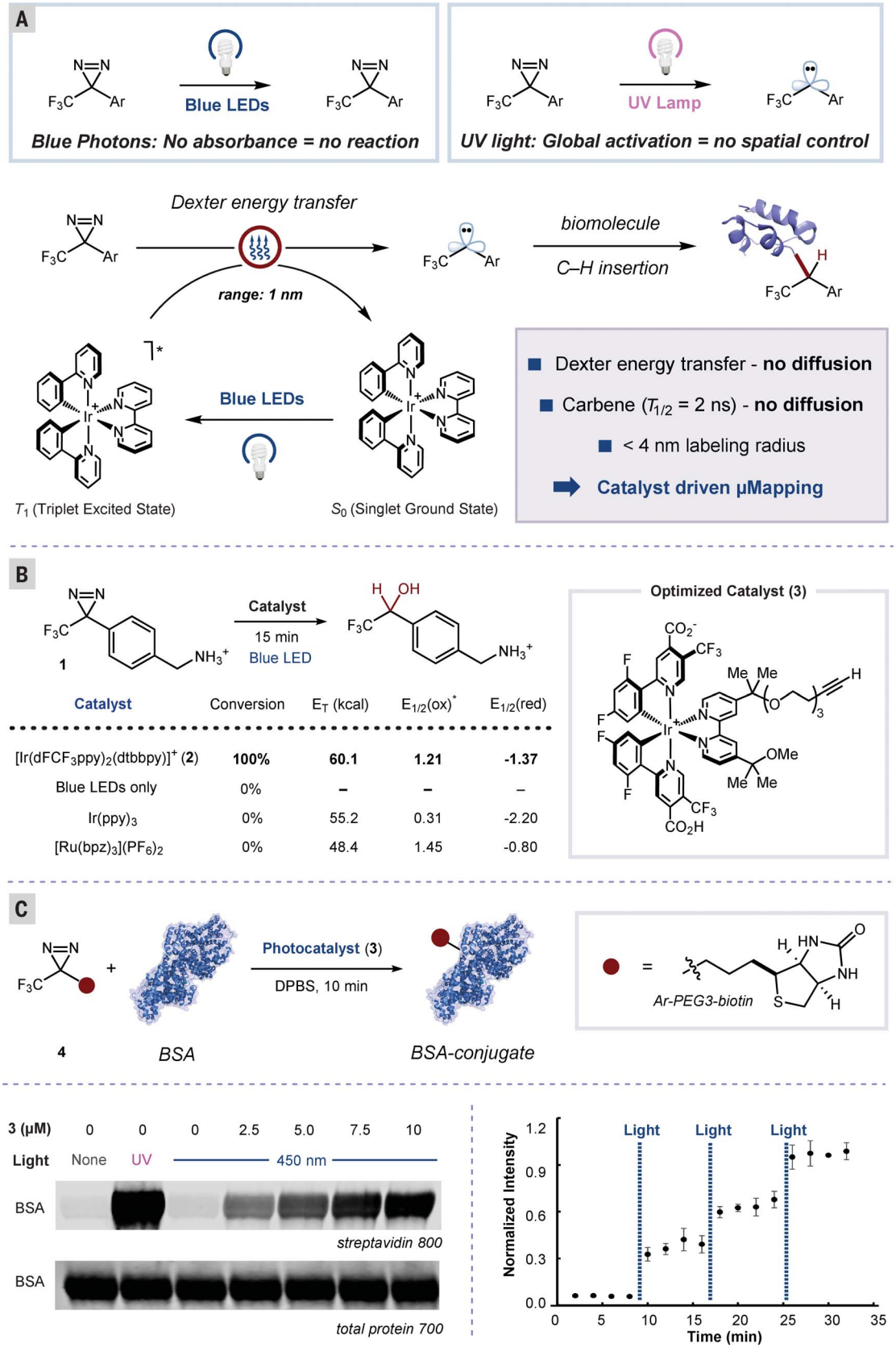

Fig. 2. Reaction design and catalyst development. (**A**) Blue light does not directly activate diazirines, whereas UV light does. In this work, we used a photocatalyst excited by using visible light for photocatalytic, energy transfer–mediated diazirine activation. (**B**) Catalyst development. Screening catalysts with a range of triplet energies demonstrated that catalytic sensitization of diazirines was possible. Catalytic activity requires a triplet energy (E_T) in excess of 60 kcal/mol, and catalysts with low triplet energies but high excited-state reduction or oxidation potentials were ineffective, suggesting an energy-transfer mechanism. Conversion was measured by means of ^{19}F–nuclear magnetic resonance spectroscopy. $E_{1/2}$, half-wave potential. (**C**) (Left) Western blot analysis of photocatalytic biotinylation of bovine serum albumin (BSA) by using a diazirine biotin conjugate (SDS–polyacrylamide gel electrophoresis, streptavidin blotting). Using light as a reagent enables fine temporal control over labeling of BSA. (Right) Short-duration illumination with light can be used to control the extent of labeling of BSA over time [streptavidin blot normalized against total protein stain; error bars are standard deviations calculated from three independent replicates (n = 3)].

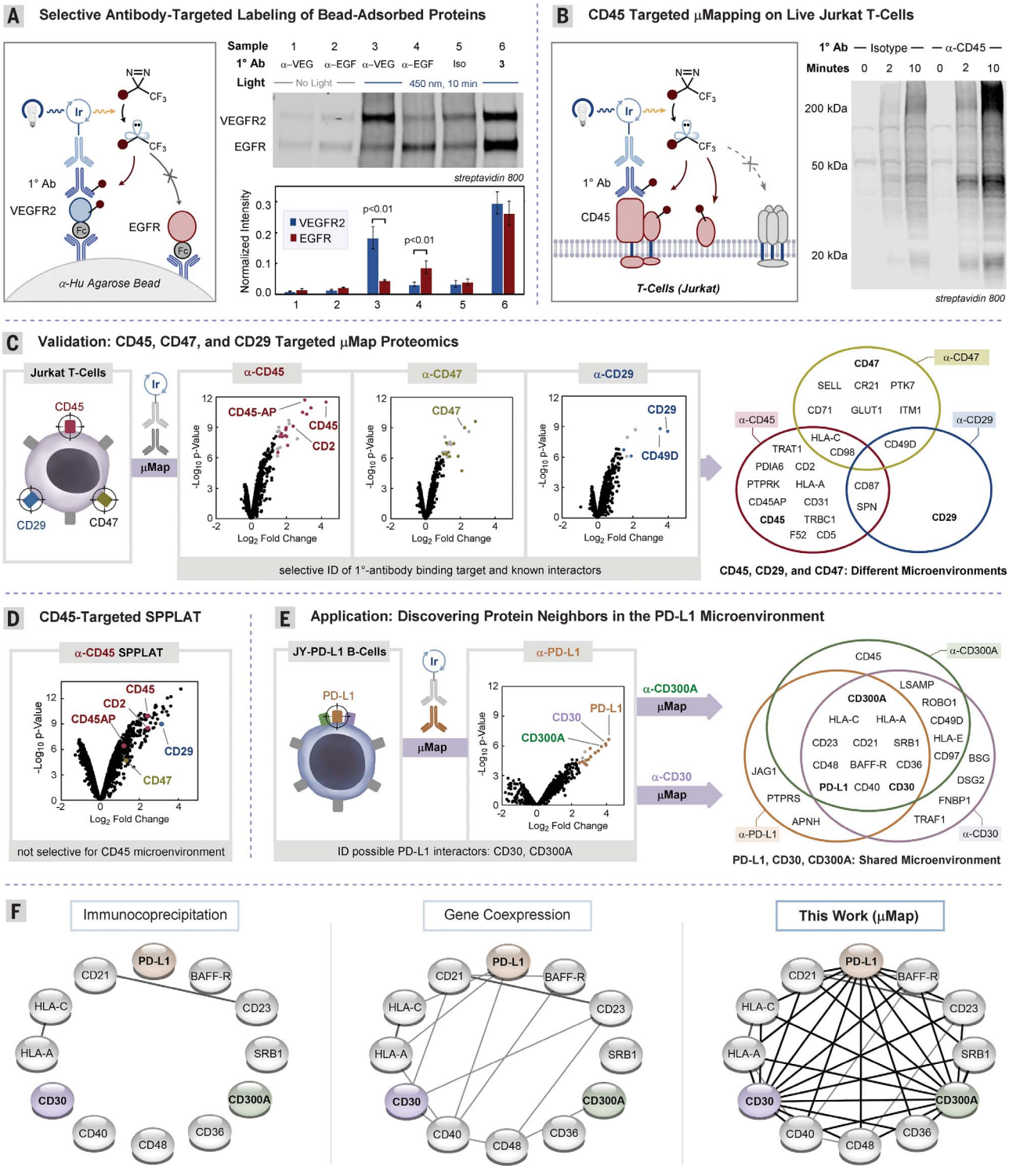

Fig. 3. μMapping on live cells. (**A**) Western blot analysis of antibody-targeted μMapping of VEGFR2-Fc or EGFR-Fc on agarose beads shows spatially selective protein labeling of VEGFR2-Fc or EGFR-Fc. Error bars in barplot are the standard deviation calculated from three independent replicates (n = 3). (**B**) Western blot analysis of antibody-targeted μMapping of CD45 on Jurkat T cells. (**C**) Selective proximity labeling of the CD45, CD47, and CD29 microenvironments using μMap. Significantly [false discovery rate (FDR)–corrected $P < 0.05$] enriched membrane proteins in volcano plots are highlighted in red (CD45), gold (CD47), or blue (CD29), and nonmembrane proteins are in gray. Venn diagram analysis of highly enriched membrane proteins shows minimal overlap. (**D**) CD45 proximity labeling on Jurkat cells by using peroxidase does not resolve CD45 and known interactors (red dots) from other proteins, including CD29 and CD47. (**E**) μMapping the PD-L1 microenvironment on JY PD-L1 B cells to reveal putative interactors. Significantly (FDR-corrected $P < 0.05$) enriched membrane proteins are highlighted in orange, and nonmembrane proteins are in gray. Labels show PD-L1 (orange), CD300A (green), and CD30 (purple) proteins. Venn diagram analysis of enriched membrane proteins shows overlap of PD-L1, CD300A, CD30, and nine other proteins. All volcano plots show averaged log2 ratios (targeted protein versus isotype) on the x axis (n = 3 replicates) and negative log10 transformed P values on the y axis. (**F**) String analysis of convergently enriched proteins.

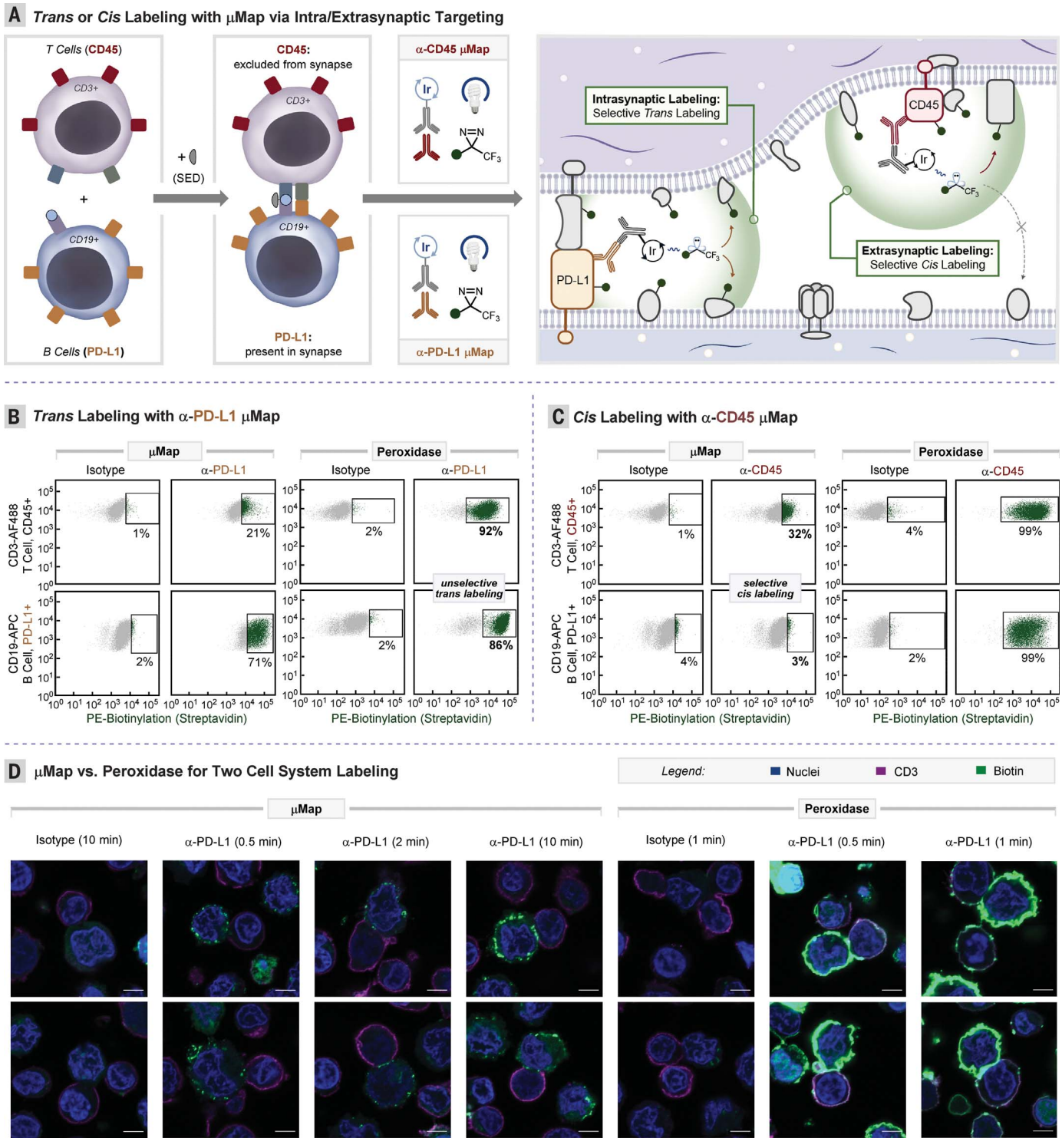

Fig. 4. Intra- and extrasynaptic μmapping within a two-cell system. (**A**) Schematic depicting Jurkat (CD45RO$^+$/PD-1$^+$/CD3$^+$) and JY (PD-L1$^+$/CD19$^+$) two-cell system enhanced by the presence of staphylococcal enterotoxin D (SED) for antibody targeting of intrasynaptic PD-L1 (expressed on JY cells) and extrasynaptic CD45RO (distinctly expressed on Jurkat cells) for selective trans or cis labeling. (**B**) Flow cytometry analysis of antibody targeting of PD-L1 on JY PD-L1 B cells with μMap by using 10-min light irradiation (left) shows both cis- and trans-cellular labeling. Peroxidase-based targeted labeling for 0.5 min (right) results in nearly complete cis- and trans-cellular labeling. (**C**) Flow cytometry analysis of antibody targeting of CD45RO on Jurkat T cells with μMap by using 10-min light irradiation (left) shows only cis-cellular labeling. Peroxidase-based targeted labeling for 0.5 min (right) results in nearly complete cis- and trans-cellular labeling. (**D**) Two-cell system confocal microscopy images of isotype-targeted (10-min light irradiation) or PD-L1–targeted (0.5-, 2-, or 10-min light irradiation) by using μMap (left) or isotype-targeted (1 min) or PD-L1–targeted (0.5 or 1 min) by using peroxidase-based labeling (right). Cells were imaged for biotinylation (green), CD3 surface expression (magenta), and nuclei (blue). Scale bar, 5 μm. Duplicate images are shown below each condition.

of the level observed through UV irradiation, establishing that the diazirine presents minimal background signal at this wavelength. However, in the presence of water-soluble iridium catalyst **3** (1 μM), catalyst-dependent biotinylation of BSA was observed. Photocatalytic labeling of BSA was further confirmed through intact protein mass spectrometry (fig. S6). Unlike other enzyme-based labeling methodologies, this approach requires continuous delivery of visible light to sustain diazirine sensitization for protein labeling. Accordingly, we exploited this feature to demonstrate how turning the light source on or off affords fine temporal control over the labeling process (Fig. 2C, right).

With an efficient photocatalytic system for carbene-based protein labeling in hand, we prepared a secondary antibody-photocatalyst conjugate as a general entry point for spatially targeted photocatalytic proximity labeling on cell surfaces. A goat anti-mouse (Gt/α-Ms) antibody was first decorated with azide groups through reaction with azidobutyric acid *N*-hydroxysuccinimide ester and then conjugated to alkyne-bearing iridium catalyst **3** by means of click chemistry, resulting in an antibody-photocatalyst ratio of 1:6. Next, to address protein-targeted labeling on a surface, we prepared a model system containing human Fc-tagged vascular endothelial growth factor receptor 2 (VEGFR2) and epidermal growth factor receptor (EGFR) proteins attached to α-human immunoglobulin G (IgG) agarose beads (Fig. 3A). These beads were sequentially incubated with a Ms/α-VEGFR2 antibody and Ir-Gt/α-Ms to position the iridium catalyst close to the VEGFR2 proteins on the bead surface. Irradiation of these beads with 450-nm light in the presence of a diazirine-biotin probe afforded selective labeling of VEGFR2 over EGFR. When Ms/α-EGFR was used as the primary antibody, the selectivity of labeling was reversed. An analogous experiment, using peroxidase-based labeling, was incapable of differentiating between EGFR or VEGFR2 (fig. S7).

Microenvironment mapping on cell membranes

We next applied antibody-targeted photocatalytic diazirine activation (μMap) to the surface of live cells. For these experiments, addition of the antibody to the cell surface was maintained at 4°C to limit antibody-mediated protein cross-linking (fig. S8) (*29*, *30*). We selected CD45, a highly abundant tyrosine phosphatase on T cell surfaces involved in antigen receptor signaling (*31*), as an initial target. Western blot analysis of CD45-targeted μMap on Jurkat cells showed light- and time-dependent protein biotinylation compared with the isotype-targeting control (Fig. 3B). Next, we used tandem mass tag (TMT)–based quantitative proteomic analysis of streptavidin-enriched proteins to identify CD45 and two known associators (CD45AP and CD2) through STRING analysis as part of a wider subset of enriched cell membrane proteins (Fig. 3C) (*32*).

With proof of concept for cell surface labeling in hand, we next questioned whether μMap could differentiate between spatially separated microenvironments on the same cell membrane. To this end, we selected CD29 and CD47 as ideal targets with, to the best of our knowledge, no known co–spatial association on the cell surface. μMapping of CD45, CD29, or CD47 on Jurkat cells resulted in the enrichment of distinct sets of proteins, which included both known (CD29:CD49D, CD45:CD45AP:CD2) and previously unknown interactors (Fig. 3C). Crucially, although several proteins were shared between pairs of targeted proteins, none were shared across all three, validating the ability of μMap to discriminate between unrelated microenvironments. By contrast, when using state-of-the-art peroxidase-based proximity labeling methods (*10*, *33*), cell surface CD45 and associated proteins were not selectively resolved from CD29 or CD47 (Fig. 3D and fig. S9).

Next, we harnessed the resolution and selectivity of μMap to investigate the proximal protein interactome of programmed-death ligand 1 (PD-L1) in B cells. As has been well established, PD-L1 plays an important role in cancer cells as an immune checkpoint ligand that can accelerate tumor progression through suppression of T cell activity (*34*). In the event, PD-L1–targeted μMap revealed CD30, a member of the tumor necrosis factor receptor family (*35*), and CD300A, an immune inhibitory receptor (Fig. 3E) (*36*), as potentially new interactors based on significant enrichment. These results highlight the potential of μMapping to provide new insights with respect to the microenvironments of checkpoint proteins.

To further validate the enriched subset of proteins identified with PD-L1 μMapping, we performed targeted labeling of these two highly enriched proteins. Targeted μMapping of these proteins within the PD-L1 microenvironment should, therefore, afford similar enrichment lists, verifying their spatial association. We found that α-CD30–, α-CD300A–, and α-PD-L1–directed μMapping identified the same set of 12 surface receptors (Fig. 3F).

It is well recognized that the development of new therapeutic oncology strategies will require an understanding of the underlying mechanisms of intercellular communication, particularly within the context of T cell activation and differentiation. Furthermore, given that localization of PD-L1 is found within the T cell/antigen-presenting cell (APC) immunosynapse (at the interface between two immunointeractive cells), we hypothesized that PD-L1–directed μMapping should lead not only to biotinylation of a PD-L1–expressing APC surface (cis-labeling) but also to the biotinylation of the adjacent synaptic T cell (trans-labeling) (Fig. 4A). As a control experiment, we further posited that when targeting a protein excluded from the synapse, such as CD45RO (*37*, *38*), the diffusion-minimized radius of μMap would preclude biotinylation of the distant trans-cell membrane.

We evaluated PD-L1– and CD45-targeted μMapping in a two-cell system composed of PD-L1–expressing JY B-lymphocytes as the APC and Jurkat T-lymphocytes distinctly expressing PD-1 and the CD45RO isoform (fig. S10). Using staphylococcal enterotoxin D (SED) to facilitate T cell receptor (TCR)–major histocompatibility complex (MHC) engagement and promote B cell/T cell immune synapse formation and signaling, we assessed the ability of μMap to selectively label within intercellular synapses (Fig. 4A and fig. S11) (*39*–*41*). Flow cytometry analysis was then used to monitor the extent of cis- and trans-cellular labeling. As anticipated, PD-L1–targeted μMap resulted in both cis- and trans-cellular labeling, whereas CD45RO-targeted μMap led to selective cis-labeling on the CD45RO-expressing Jurkat cells (Fig. 4, B and C, and fig. S12), without any labeling of the adjacent B cell. In stark contrast to μMap, peroxidase-based proximity labeling of PD-L1 or CD45RO within this two-cell system led to complete labeling of both cell types within 30 s, clearly visualized through flow cytometry and confocal microscopy (Fig. 4, B, C, and D; and fig. S12). In comparison, PD-L1–targeted μMap showed high selectivity for trans-labeling solely at the cis- and trans-cellular contact regions (Fig. 4D and fig. S12). Applying the μMap technology on PD-1 in the Jurkat-JY coculture system resulted in the reciprocal trend of cis- and trans-cellular labeling (fig. S13). Collectively, these findings clearly demonstrate that the capacity of μMap to elucidate protein-protein interactions can be directly translated toward the highly selective labeling of dynamic interfaces within complex multicellular systems.

We expect that this technology will find immediate use in antibody target identification, exploration of signal transduction pathways, profiling cell-cell junctions, and other disease-relevant microenvironments.

REFERENCES AND NOTES

1. E. Lundberg, G. H. H. Borner, *Nat. Rev. Mol. Cell Biol.* **20**, 285–302 (2019).
2. N. C. Bauer, P. W. Doetsch, A. H. Corbett, *Traffic* **16**, 1039–1061 (2015).
3. B. Z. Stanton, E. J. Chory, G. R. Crabtree, *Science* **359**, eaao5902 (2018).
4. R. R. Minter, A. M. Sandercock, S. J. Rust, *Drug Discov. Today. Technol.* **23**, 83–90 (2017).
5. D. S. Johnson, A. Mortazavi, R. M. Myers, B. Wold, *Science* **316**, 1497–1502 (2007).
6. M. Hanoun, M. Maryanovich, A. Arnal-Estapé, P. S. Frenette, *Neuron* **86**, 360–373 (2015).
7. S. S. Lam *et al*., *Nat. Methods* **12**, 51–54 (2015).
8. J. S. Rees, X.-W. Li, S. Perrett, K. S. Lilley, A. P. Jackson, *Mol. Cell. Proteomics* **14**, 2848–2856 (2015).
9. N. Hashimoto *et al*., *Proteomics* **12**, 3154–3163 (2012).
10. J. S. Rees, X.-W. Li, S. Perrett, K. S. Lilley, A. P. Jackson, *Curr. Protoc. Protein Sci.* **80**, 19.27.11–19.27, 18 (2015).
11. E. Choi-Rhee, H. Schulman, J. E. Cronan, *Protein Sci.* **13**, 3043–3050 (2004).
12. L. K. Folkes, M. Trujillo, S. Bartesaghi, R. Radi, P. Wardman, *Arch. Biochem. Biophys.* **506**, 242–249 (2011).
13. H.-W. Rhee *et al*., *Science* **339**, 1328–1331 (2013).

14. D. I. Kim *et al.*, *Proc. Natl. Acad. Sci. U.S.A.* **111**, E2453–E2461 (2014).
15. K. Bersuker *et al.*, *Dev. Cell* **44**, 97–112.e7 (2018).
16. K. H. Loh *et al.*, *Cell* **166**, 1295–1307.e21 (2016).
17. D. Z. Bar *et al.*, *Nat. Methods* **15**, 127–133 (2018).
18. D. Z. Bar *et al.*, *Nat. Methods* **15**, 749 (2018).
19. X.-W. Li *et al.*, *J. Biol. Chem.* **289**, 14434–14447 (2014).
20. N. Kotani *et al.*, *Proc. Natl. Acad. Sci. U.S.A.* **105**, 7405–7409 (2008).
21. T. Hayashi, Y. Yasueda, T. Tamura, Y. Takaoka, I. Hamachi, *J. Am. Chem. Soc.* **137**, 5372–5380 (2015).
22. A. Admasu *et al.*, *J. Chem. Soc., Perkin Trans. 2* (5): 1093–1100 (1998).
23. H. C. Berg, *Random Walks in Biology* (Princeton Univ. Press, 1993).
24. S.-S. Ge *et al.*, *RSC Adv.* **8**, 29428 (2018).
25. J. Brunner, H. Senn, F. M. Richards, *J. Biol. Chem.* **255**, 3313–3318 (1980).
26. D. M. Arias-Rotondo, J. K. McCusker, *Chem. Soc. Rev.* **45**, 5803–5820 (2016).
27. J. Wang, J. Kubicki, H. Peng, M. S. Platz, *J. Am. Chem. Soc.* **130**, 6604–6609 (2008).
28. A. Singh *et al.*, *J. Organomet. Chem.* **776**, 51–59 (2015).
29. L. Y. Bourguignon, S. J. Singer, *Proc. Natl. Acad. Sci. U.S.A.* **74**, 5031–5035 (1977).
30. L. Y. Bourguignon, *J. Cell Biol.* **83**, 649–656 (1979).
31. M. L. Hermiston, Z. Xu, A. Weiss, *Annu. Rev. Immunol.* **21**, 107–137 (2003).
32. D. Szklarczyk *et al.*, *Nucleic Acids Res.* **47** (D1), D607–D613 (2019).
33. V. Hung *et al.*, *Nat. Protoc.* **11**, 456–475 (2016).
34. H. O. Alsaab *et al.*, *Front. Pharmacol.* **8**, 561 (2017).
35. C. A. van der Weyden, S. A. Pileri, A. L. Feldman, J. Whisstock, H. M. Prince, *Blood Cancer J.* **7**, e603 (2017).
36. O. Zenarruzabeitia, J. Vitallé, C. Eguizabal, V. R. Simhadri, F. Borrego, *J. Immunol.* **194**, 5053–5060 (2015).
37. J. R. James, R. D. Vale, *Nature* **487**, 64–69 (2012).
38. C. B. Carbone *et al.*, *Proc. Natl. Acad. Sci. U.S.A.* **114**, E9338–E9345 (2017).
39. M. L. Dustin, *Cancer Immunol. Res.* **2**, 1023–1033 (2014).
40. I. V. Pinchuk, E. J. Beswick, V. E. Reyes, *Toxins (Basel)* **2**, 2177–2197 (2010).
41. M. C. Montoya *et al.*, *Nat. Immunol.* **3**, 159–168 (2002).
42. C. White, R. Oslund, O. Fadeyi, T. Reyes Robles, Flow cytometry data files for article: Microenvironment mapping via Dexter energy transfer on immune cells. Harvard Dataverse (2020).
43. C. White, Merck/Photoproximity_Labeling: Photoproximity_Labeling_v1.0. Zenodo (2020).

ACKNOWLEDGMENTS

We thank A. D. Trowbridge and C. P. Seath for their assistance with the preparation of this manuscript and D. Hazuda for insightful comments and suggestions. We also thank Efficiency Aggregators for development of the biophotoreactor used in this work.
Funding: Research reported in this publication was supported by the NIH National Institute of General Medical Sciences (R01-GM103558-03) and gifts from Merck & Co., Inc., Kenilworth, New Jersey, USA. J.B.G. acknowledges the NIH for a postdoctoral fellowship (F32-GM133133-01). J.V.O. acknowledges the NSF for a predoctoral fellowship (DGE-1656466). **Author contributions:** D.W.C.M., R.C.O., O.O.F., and S.J.M. conceived of the work. J.B.G., J.V.O., T.W., R.C.O., O.O.F., T.R.-R., and C.H.W. designed and executed experiments. D.L.P., F.P.R.-R., and E.C.H. provided insight and direction for experimental design. **Competing interests:** J.B.G., J.V.O., T.W., R.C.O., O.O.F., and D.W.C.M. have filed a provisional U.S. patent application on this work. **Data and materials availability:** Raw flow cytometry data are available through the Harvard Dataverse (*42*). Code for replicating proteomic data analysis, generation of volcano plots, and raw peptide level abundance data for each of the experiments are available in a GitHub repository (*43*). All other data are available in the main text or the supplementary materials.

SUPPLEMENTARY MATERIALS

science.sciencemag.org/content/367/6482/1091/suppl/DC1
Materials and Methods
Figs. S1 to S51
Table S1
References (*44*–*58*)
Data File S1

View/request a protocol for this paper from *Bio-protocol*.

16 June 2019; resubmitted 13 November 2019
Accepted 6 February 2020
10.1126/science.aay4106

Microenvironment mapping via Dexter energy transfer on immune cells

Jacob B. Geri, James V. Oakley, Tamara Reyes-Robles, Tao Wang, Stefan J. McCarver, Cory H. White, Frances P. Rodriguez-Rivera, Dann L. Parker Jr., Erik C. Hett, Olugbeminiyi O. Fadeyi, Rob C. Oslund and David W. C. MacMillan

Science **367** (6482), 1091-1097.
DOI: 10.1126/science.aay4106

Pinpointing proteins

To develop drugs that target a specific cell surface protein, it's helpful to know which other proteins reside in its vicinity. Geri *et al.* report a light-triggered labeling technique that improves the spatial resolution for this type of mapping. Specifically, they rely on a photocatalyst with a very short energy-transfer range to activate a carbene-based label that can only diffuse a short distance in water before reacting. They showcase the technique by mapping the environment of the programmed-death ligand 1 (PDL1) protein on B cell surfaces, a system of considerable interest in cancer immunotherapy.

Science, this issue p. 1091